WEP Warwick Evans Publishing

International Journal of Computer Science and Information Technology

ISSN: 3005-9682 (Print), ISSN: 3005-7140 (Online) | Volume 8, Number 2, Year 2026
DOI: https://doi.org/10.62051/ijcsit.v8n2.07
Journal homepage: https://wepub.org/index.php/IJCSIT/index

Transfer Learning-Based Electromagnetic Inversion for LWD

Zhen Li

School of Physics & Electronic infarmation Engineering, Henan Polytechnic University, Jiaozuo, China

ABSTRACT

Three-dimensional inversion of logging-while-drilling (LWD) data serves as a key technology for boundary detection and reservoir characterization under complex geological conditions. Currently, inversion methods based on deep neural networks are prone to overfitting, often yielding unreliable results when training samples are limited. To address this issue, this paper proposes a transfer learning-based electromagnetic inversion approach for LWD, adopting a strategy of 2D pre-training followed by 3D fine-tuning. This strategy enables efficient transfer of electromagnetic features learned from 2D models to 3D networks, thereby reducing the dependency of 3D inversion on large-scale datasets. Furthermore, a Bayesian Neural Network (BNN) is integrated to construct a unified 3D inversion framework, achieving simultaneous prediction of resistivity distribution and quantification of uncertainty. Numerical experiments demonstrate that the proposed method achieves fast and stable convergence even with a limited number of 3D training samples, while maintaining high inversion accuracy under varying noise levels. In addition, uncertainty estimation effectively reveals the impact of inadequate prior knowledge and noise interference on the inversion results. By ensuring inversion accuracy and significantly improving computational efficiency, the proposed method provides robust technical support for electromagnetic LWD inversion in complex geological settings.

KEYWORDS

Logging-while-drilling electromagnetic; Three-dimensional inversion; Transfer learning; Bayesian neural network

1. INTRODUCTION

With the increasing dimensionality and complexity of logging-while-drilling (LWD) data, deep learning (DL)-based inversion methods have gradually emerged as a significant research focus in the field of LWD electromagnetic interpretation [1]. In contrast to conventional iterative inversion approaches, which heavily rely on explicit physical modeling and numerical optimization, deep learning techniques construct a nonlinear mapping relationship between measured responses and formation parameters. This framework bypasses repetitive forward modeling computations and enables rapid prediction of resistivity structures, thereby enhancing both the real-time performance and computational efficiency of LWD electromagnetic interpretation [2].

In recent years, more and more scholars have studied deep learning algorithms to solve the problem of electromagnetic inversion while drilling [3, 4], especially in terms of datasets [5], network architecture [6] and loss function [7], and have made significant progress. In the study of electromagnetic inversion while drilling, most early studies assumed that the underground medium was a one-dimensional layered structure, that is, the formation resistivity only changed along the well depth direction and remained homogeneous in the horizontal direction [8, 9]. Puzyrev [10] et al. proposed a method to estimate the underground resistivity distribution using convolutional neural

networks for anomalies under the one-dimensional layered model, which verified the feasibility and efficiency of deep learning in the electromagnetic inversion problem. Hu [11] et al. used a supervised descent method combined with deep learning to solve the problem of electromagnetic directional logging inversion while drilling, which significantly improved the inversion speed and stability under the one-dimensional formation model. K. Noh [12] et al. introduced Bayesian Neural Network (BNN) into one-dimensional electromagnetic inversion while drilling, and realized the unified modeling of resistivity parameter prediction and uncertainty quantification. Zhao et al. [13] proposed that by introducing electromagnetic physical constraints and using physical-driven deep learning methods, the robustness and generalization ability of the model under noise conditions were improved. The above studies show that under the assumption of one-dimensional layered strata, machine learning and deep learning methods can achieve high-precision and high-efficiency drilling electromagnetic inversion. However, the one-dimensional model ignores key geological features such as stratum dip angle, faults and lateral heterogeneity, and is difficult to adapt to the complex structural environment that is common in actual drilling electromagnetic inversion. Its generalization ability and scope of application are significantly limited, which has also promoted the inversion research of two-dimensional strata models to gradually deepen [14]. Noh et al. [15] constructed a deep learning inversion framework for two-dimensional strata models containing faults, and realized the rapid prediction of two-dimensional resistivity distribution of the wellbore from multi-frequency and multi-spacing drilling electromagnetic measurement data, which verified the effectiveness of deep learning under complex structural conditions. Zhao et al. [16] proposed a hybrid inversion process that couples physical driving and deep learning to solve the 2D resistivity problem of LWD. By integrating physical information into the DL scheme, the inversion performance was significantly improved. Qin et al. [17] designed a deep learning model based on a bidirectional long short-term memory network to invert LWD azimuth electromagnetic data and realize the rapid estimation of two-dimensional formation parameters. The experimental results show that its accuracy under noise interference is better than that of traditional methods. Compared with the one-dimensional assumption, two-dimensional machine learning inversion can more accurately characterize the geometric morphology and electrical changes of the formation, providing a new technical path for drilling electromagnetic interpretation in complex tectonic environments [18]. However, the two-dimensional model still assumes that the formation changes in a single direction, which makes it difficult to fully describe the three-dimensional heterogeneous characteristics of the real underground medium. Its inversion results are essentially still an approximation of the three-dimensional problem, which is also an important reason for further developing three-dimensional drilling electromagnetic inversion methods.

At present, research on three-dimensional electromagnetic inversion in the field of electromagnetic drilling is relatively limited, mainly due to two core challenges: First, the scarcity of three-dimensional labeled data and the high cost of training. The complex electromagnetic response of three-dimensional strata needs to generate data through fine grid simulation. The simulation time of a single sample is several times that of two-dimensional simulation, making it difficult to obtain large-scale labeled samples. This puts extremely high demands on computing resources and the efficiency of inversion algorithms [19, 20]. The generalization ability of machine learning models is highly dependent on sufficient data. Directly training three-dimensional models often falls into underfitting or extremely low training efficiency due to insufficient data. Therefore, it is necessary to develop technologies that can significantly reduce the data requirements and training costs of three-dimensional inversion [21]. In response to this problem, this paper adopts data-efficient utilization technology such as transfer learning. Puzyrev [22] et al. proposed that transfer learning can significantly reduce the dependence of the target task on large-scale labeled data by transferring the knowledge learned in the source domain to the target domain. It has been proven to be an effective means to overcome the problem of high dimension and high computational cost in multiple geophysical inversion fields. Yosinski [23] et al. showed that when the feature distributions of the source domain and the target domain are highly overlapping, transfer learning can reduce the amount of labeled data required for the target task by 70% to 95%. Zhang et al. [24] also achieved a leapfrog

compression of training data from hundreds of thousands to thousands in three-dimensional seismic waveform inversion and three-dimensional gravity and magnetic inversion. In this study, the consistency of physical mechanisms and partial overlap of parameter spaces between two-dimensional and three-dimensional data were utilized to enable three-dimensional electromagnetic inversion while drilling to achieve high-precision convergence with only tens of thousands of samples, providing a practical solution to the problem of limited computing resources in real-time geological exploration scenarios. However, traditional transfer learning frameworks focus on feature transfer and model performance improvement, and it is difficult to quantify the uncertainty of inversion results.

Secondly, the actual measurement environment of electromagnetic inversion while drilling is extremely complex. Drilling tool structure, drilling fluid properties, wellbore morphology and formation heterogeneity will strongly interfere with electromagnetic wave propagation, resulting in signal distortion and a significant decrease in signal-to-noise ratio [25, 26]. At the same time, the sensor position is constantly changing, and the electromagnetic field coupling effect is strong, which makes the inversion algorithm often have problems of convergence difficulty and insufficient stability when dealing with complex media [27, 28]. These unavoidable measurement disturbances bring about multi-source uncertainties, making it difficult to evaluate the credibility of the inversion results. Therefore, an inversion framework that can quantify uncertainties is needed. This shortcoming can be made up by Bayesian neural networks, so this paper introduces this network. This network was proposed in the field of deep learning [29], and its performance was evaluated by two extended methods of uncertainty estimation [30], namely cognitive uncertainty and arbitrary uncertainty. Seokmin and Joongmoo proposed a method for estimating uncertainty in electromagnetic data deep inversion based on a Bayesian framework [31]. Through iterative estimation of convolutional neural networks with dropout, cognitive and arbitrary uncertainties as well as resistivity models are provided.

The innovation of this paper lies in its construction of a technical framework integrating transfer learning and Bayesian neural networks to address the two problems of data scarcity and uncertainty quantification in 3D drilling electromagnetic inversion. On the one hand, leveraging the similarity between 2D and 3D models in physical mechanisms and parameter spaces, a 2D pre-training—3D fine-tuning transfer strategy is designed to reduce the 3D model's dependence on large-scale labeled data. On the other hand, through the deep integration of BNN and transfer learning, efficient inversion is achieved while simultaneously quantifying cognitive and arbitrary uncertainties, overcoming the shortcoming of traditional transfer learning in providing credibility assessment. This results in an integrated inversion scheme that combines high efficiency, cost reduction, and quantitative reliability, providing an engineeringable technical path for real-time geological exploration under complex geological conditions.

2. THEORETICAL BASIS

2.1. Inversion Workflow

This paper constructs the whole flow of electromagnetic 3D inversion while drilling, which covers data construction, pre-training, migration adaptation, 3D modeling and uncertainty analysis, as shown in Figure 1. Firstly, the framework uses fault and fault-free models of 2D data to construct source domain dataset for pre-training, and extracts physically consistent electromagnetic features. In this paper, 2D knowledge is effectively transferred to 3D network by freezing the bottom shared layer, fine-tuning the middle layer and adding training dip parameter branches, which reduces the dependence on large-scale 3D labeled data. On this basis, 3D data sets with different noise levels are introduced to fine-tune 3D networks, and resistivity parameters, cognitive uncertainties (reflecting insufficient data coverage) and arbitrary uncertainties (reflecting noise interference) are output simultaneously. In order to achieve accurate inversion of complex geological bodies, this paper adopts the strategy of subarea inversion and result combination to accurately recover the discontinuous

boundary and dip characteristics of complex fault graben model. Uncertainty analysis further reveals the mechanism of reducing cognitive uncertainty with increasing data volume and amplifying arbitrary uncertainty with increasing noise. In this paper, the coefficient of determination and RMS error are used to further evaluate the predicted model parameters, which provides an efficient, credible and engineerable inversion technology path for real-time geological exploration under complex geological conditions.

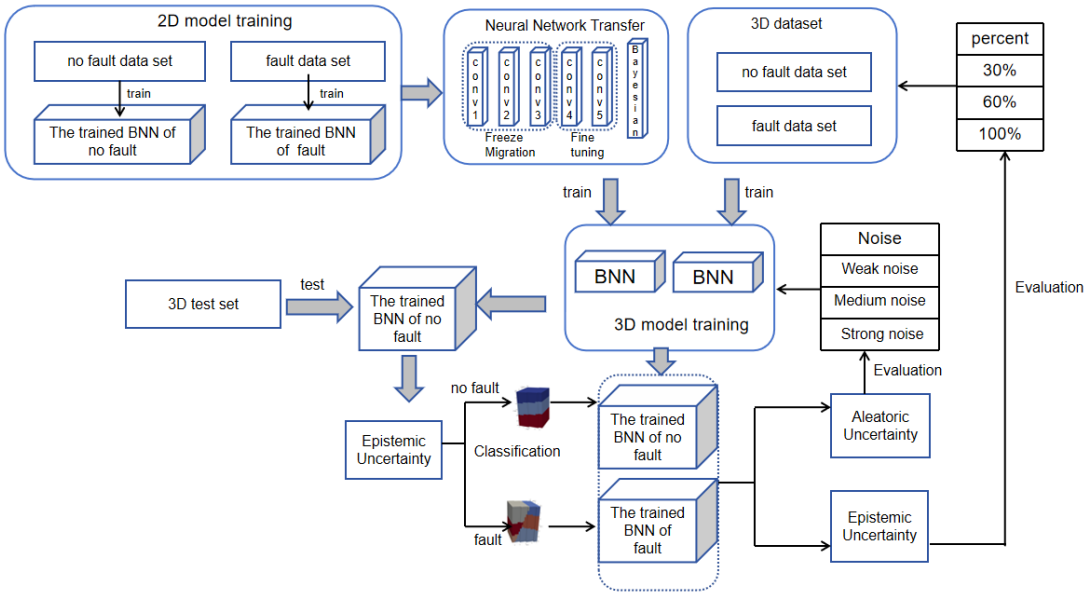

Figure 1. Flow chart of electromagnetic migration while drilling learning inversion

2.2. Transfer Learning

3D electromagnetic inversion while drilling faces the challenge of scarce labeled data and high simulation cost: 3D model needs fine grid to captureXY plane dip, resulting in multiple times of calculation time per sample compared with 2D. Therefore, transfer learning strategy is adopted to reduce the requirement of three-dimensional data significantly by taking advantage of the consistency of physical mechanism and partial overlap of parameter space between two-dimensional (source domain) and three-dimensional (target domain) models. Through 2D pre-training-3D fine-tuning framework, 2D knowledge is efficiently transferred to 3D BNN, and training samples are compressed from traditional millions to tens of thousands, while avoiding negative transfer risk.

Let the source-domain dataset be (2D electromagnetic response-to-parameter mapping) and the target domain be (3D,). The network parameters are decomposed into shared layers (common characteristics of the bottom layer, independent of dip), source domain specific layers (parameters specific to the 2D model) and target domain specific layers (new dip branching parameters for the 3D model). Pre-training phase: Minimize source domain loss on:

$$\mathscr{L}_S(\theta_{shared}, \theta_S)=\frac{1}{N_S}\sum_{i=1}^{N_S} \ell\left(f(x_S^i; \theta_{shared}, \theta_S), y_S^i\right) \quad (1)$$

Where is the mean square error. Fine-tuning phase: Freeze (direct migration), fine-tune the upper middle layer and train to minimize target domain loss:

$$\mathscr{L}_T(\theta^*_{shared}, \theta_T)=\frac{1}{N_T}\sum_{j=1}^{N_T} \ell\left(f(x_T^j; \theta^*_{shared}, \theta_T), y_T^j\right)+\lambda\mathscr{R}(\theta_T) \quad (2)$$

Where is the pre-training parameter, and is the regularization term to prevent overfitting and control the migration intensity.

In this paper, two dimensional (source domain) and three dimensional (target domain) neural networks have core commonalities: the input data dimensions are similar, the reconstruction target is highly consistent, and the common characteristics of the bottom layer (conv1-x to conv3-x of ResNet50) are independent of tilt angle, and the similarity increases from bottom to top. Therefore, we adopt a transfer learning strategy: 2D network as a pre-trained model of 3D network, freezing the direct transfer of the bottom layer, fine-tuning the middle layer (conv4-x) and the top layer (conv5-x), and adding a new tilt parameter branch to the BNN.

2.3. Bayesian Neural Network

Electromagnetic inversion while drilling (ELWD) is a nonlinear inverse problem with high dimension. Influenced by formation complexity and observation noise, inversion results have significant uncertainty. Traditional deterministic neural networks output only point estimates and cannot quantify model confidence or distinguish cognitive uncertainty from arbitrary uncertainty. In this paper, Bayesian neural network (BNN) is used to construct a 3D inversion model, and weights are considered as random variables to realize the joint modeling of resistivity prediction and uncertainty.

The posterior distribution of BNN is given by Bayesian formula:

$$p(\omega|D)=\frac{p(D|\omega)p(\omega)}{p(D)} \tag{3}$$

Where is the dataset; is the Gaussian prior; is the likelihood function. For new input data, the predicted distribution is:

$$p(y^*|x^*, D)=\int p(y^*|x^*, \omega)\, p(\omega|D)d\omega \tag{4}$$

Since the posterior is not analytic, this paper uses variational reasoning approximation: introduce a variational distribution (parameterized to Gaussian) to minimize divergence.

Equivalent to maximizing evidence lower bound (ELBO):

$$ELBO(\theta)=E_q[\log p(D|\omega)]-KL\left(q_\theta(\omega)\|p(\omega)\right) \tag{5}$$

The first term facilitates data fitting and the second term regularizes against overfitting. In training, reparameterization techniques such as making the sampling process differentiable support backpropagation optimization.

After training, prediction means and variances are calculated by subsampling:

$$\bar{y}=\frac{1}{T}\sum_{t=1}^{T} f\left(x^*; w^{(t)}\right),\ \sigma^2=\frac{1}{T}\sum_{t=1}^{T}\left(f\left(x^*; w^{(t)}\right)\right)^2-\bar{y}^2 \tag{6}$$

The variance is decomposed into:

$$\sigma^2=\underbrace{E_q[Var(y|x, \omega)]}_{\text{Aleatoric Uncertainty}}+\underbrace{Var_q[E(y|x, \omega)]}_{\text{Epistemic Uncertainty}} \tag{7}$$

Cognitive uncertainty decreases with increasing three-dimensional samples and is used to identify out-of-distribution structures such as faults. Arbitrary uncertainty is positively correlated with noise intensity and is used to evaluate LWD measurement interference.

3. DATA SET CONSTRUCTION AND TRAINING METHODS

3.1. Dataset Builder

The fault-free model is shown in Figure 2(a). The 3D fault-free model is randomly generated by parameterizing eight variables. These 8 variables are resistivity values of three dipping layers, sum of two dip angles of layer boundary in YZ plane $\theta_u\theta_l$, dip angle of XY plane θ_t, sum of two vertical distances from layer boundary to horizontal center of local logging trace d_ud_l.

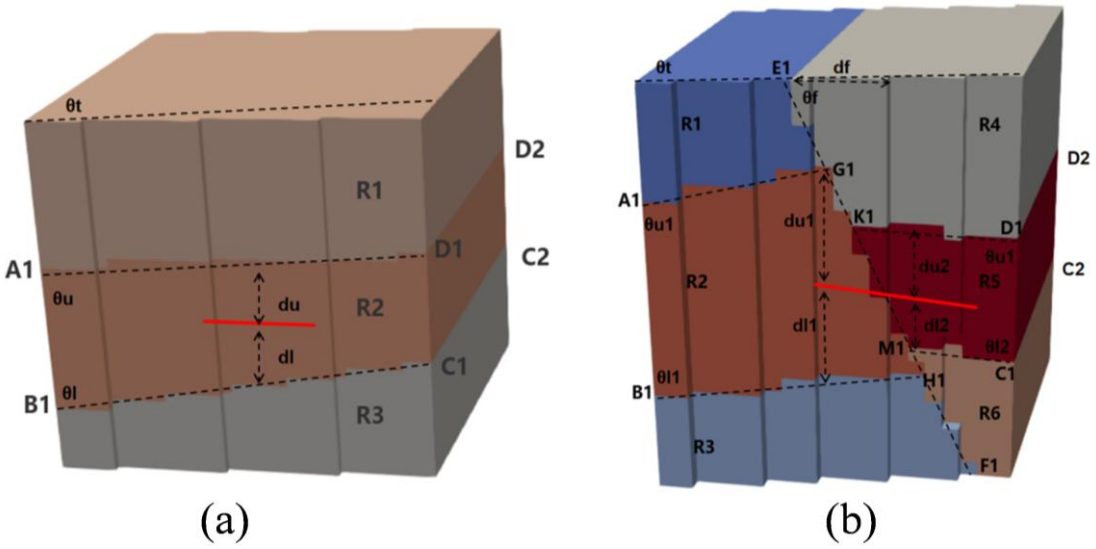

Figure 2. Schematic diagram of parameters of two models (a) fault-free model; (b) fault model

The fault model is shown in Figure 2(b). The 3D fault model is randomly generated by parameterizing 17 variables. These 17 variables are resistivity values of 6 inclined layers, dip angles of YZ plane boundary, dip angles of XY plane, vertical distances from formation boundary to horizontal center of local logging trace, dip angles of faults and horizontal distances from upper boundary of faults to horizontal center of local logging trace. The parameter changes of the two models are shown in Table 1.

Table 1. Parameter variation range of 3D fault-free and fault models

Resistivity value/()	Distance from logging to boundary/m	YZ plane inclination/°	XY plane inclination/°	Horizontal distance of fault plane/m	Fault dip/°
[0.1, 100.0]	[1.0, 10.0]	[70, 110]	[70, 110]	[0.0, 3.0]	[70, 110]

Considering the generation of data set without fault model in Figure 2(a), convert variable settings into coordinate settings of eight moving points A1, B1, C1, D1, A2, B2, C2 and D2, and their expressions are shown in Table 2. According to the fault model in Figure 2(b), convert variable settings into coordinate settings of twenty moving points A1, B1, C1, D1, E1, F1, G1, K1, H1, M1, A2, B2, C2, D2, E2, F2, G2, K2, H2 and M2, and their expressions are shown in Table 3. Bychanging the set points and connectingthe corresponding points, fault-free and fault modelscan beconstructed.

Table 2. Expressions of moving points and coordinates of 3-D fault-free model

moving point	Moving point coordinate expression
A1	$(10.0, -10.0, -(15.0-d_u+10.0*\tan\theta_u))$
B1	$(10.0, -10.0, -(15.0+d_l+10.0*\tan\theta_l))$
C1	$(10.0-20.0*\tan\theta_t, 10.0, -(15.0+d_l-10.0*\tan\theta_l))$
D1	$(10.0-20.0*\tan\theta_t, 10.0, -(15.0-d_u-10.0*\tan\theta_u))$
A2	$(-10.0, -10.0, -(15.0-d_u+10.0*\tan\theta_u))$
B2	$(-10.0, -10.0, -(15.0+d_l+10.0*\tan\theta_l))$
C2	$(-10.0-20.0*\tan\theta_t, 10.0, -(15.0+d_l-10.0*\tan\theta_l))$
D2	$(-10.0-20.0*\tan\theta_t, 10.0, -(15.0-d_u-10.0*\tan\theta_u))$

Table 3. Expressions of moving points and coordinates of three-dimensional fault model

moving point	Moving point coordinate expression
A1	$(10.0, -10.0, -((10.0-\|G1\_Y\|)*\tan\theta_{u1}+\|G1\_Z\|))$
B1	$(10.0, -10.0, -((10.0+\|H1\_Y\|)*\tan\theta_{l1}+\|H1\_Z\|))$
C1	$(10.0-20.0*\tan\theta_t, 10.0, -((10.0-\|M1\_Y\|)*\tan\theta_{l2}+\|M1\_Z\|))$
D1	$(10.0-20.0*\tan\theta_t, 10.0, -((10.0-\|K1\_Y\|)*\tan\theta_{l2}+\|K1\_Z\|))$
E1	$(10.0-(E1\_Y+10.0)*\tan\theta_t, -d_f, 0.0)$
F1	$(10.0-(F1\_Y+10.0)*\tan\theta_t, 30.0*\tan(\frac{\pi}{2}-\theta_f)-d_f, -30.0)$
G1	$(10.0-(G1\_Y+10.0)*\tan\theta_t, (15.0-d_{u1})*\tan(\frac{\pi}{2}-\theta_f)-d_f, -(15.0-d_{u1}))$
K1	$(10.0-(K1\_Y+10.0)*\tan\theta_t, (15.0-d_{u2})*\tan(\frac{\pi}{2}-\theta_f)-d_f, -(15.0-d_{u2}))$
H1	$(10.0-(H1\_Y+10.0)*\tan\theta_t, (15.0+d_{l1})*\tan(\frac{\pi}{2}-\theta_f)-d_f, -(15.0+d_{l1}))$
M1	$(10.0-(M1\_Y+10.0)*\tan\theta_t, (15.0+d_{l2})*\tan(\frac{\pi}{2}-\theta_f)-d_f, -(15.0+d_{l2}))$
A2	$(-10.0,-10.0, -((10.0-\|G1\_Y\|)*\tan\theta_{u1}+\|G1\_Z\|))$
B2	$(-10.0,-10.0, -((10.0+\|H1\_Y\|)*\tan\theta_{l1}+\|H1\_Z\|))$
C2	$(-10.0-20.0*\tan\theta_t, 10.0, -((10.0-\|M1\_Y\|)*\tan\theta_{l2}+\|M1\_Z\|))$
D2	$(-10.0-20.0*\tan\theta_t, 10.0, -((10.0-\|K1\_Y\|)*\tan\theta_{l2}+\|K1\_Z\|))$
E2	$(-10.0-(E1\_Y+10.0)*\tan\theta_t, -d_f, 0.0)$
F2	$(-10.0-(F1\_Y+10.0)*\tan\theta_t, 30.0*\tan(\frac{\pi}{2}-\theta_f)-d_f, -30.0)$
G2	$(-10.0-(G1\_Y+10.0)*\tan\theta_t, (15.0-d_{u1})*\tan(\frac{\pi}{2}-\theta_f)-d_f, -(15.0-d_{u1}))$
K2	$(-10.0-(K1\_Y+10.0)*\tan\theta_t, (15.0-d_{u2})*\tan(\frac{\pi}{2}-\theta_f)-d_f, -(15.0-d_{u2}))$
H2	$(-10.0-(H1\_Y+10.0)*\tan\theta_t, (15.0+d_{l1})*\tan(\frac{\pi}{2}-\theta_f)-d_f, -(15.0+d_{l1}))$
M2	$(-10.0-(M1\_Y+10.0)*\tan\theta_t, (15.0+d_{l2})*\tan(\frac{\pi}{2}-\theta_f)-d_f, -(15.0+d_{l2}))$

3.2. Network Training Process

In this study, 10000 three-dimensional samples were constructed by numerical simulation and divided into training set and test set according to the ratio of 8:2, which were used for model training and performance verification respectively. Based on SimPEG numerical simulation tool, the amplitude and phase parameters of electromagnetic response of the model are calculated and obtained. The amplitude ratio and phase difference are used as input characteristics of the network, and the model

parameters are used as output target labels. The neural network training is carried out based on TensorFlow framework. As shown in Figure 3, when transfer learning is not used, after 1000 iterations of training data of the same size, the loss function only converges to 0.1 magnitude, and it is difficult to achieve effective prediction. After 2D pretraining-3D fine-tuning transfer learning strategy is adopted, only 200 iterations are needed, and the loss value is stable at 0.001 magnitude. The prediction results are shown in Figure 4. The network optimized by transfer learning can achieve high accuracy and effective prediction.

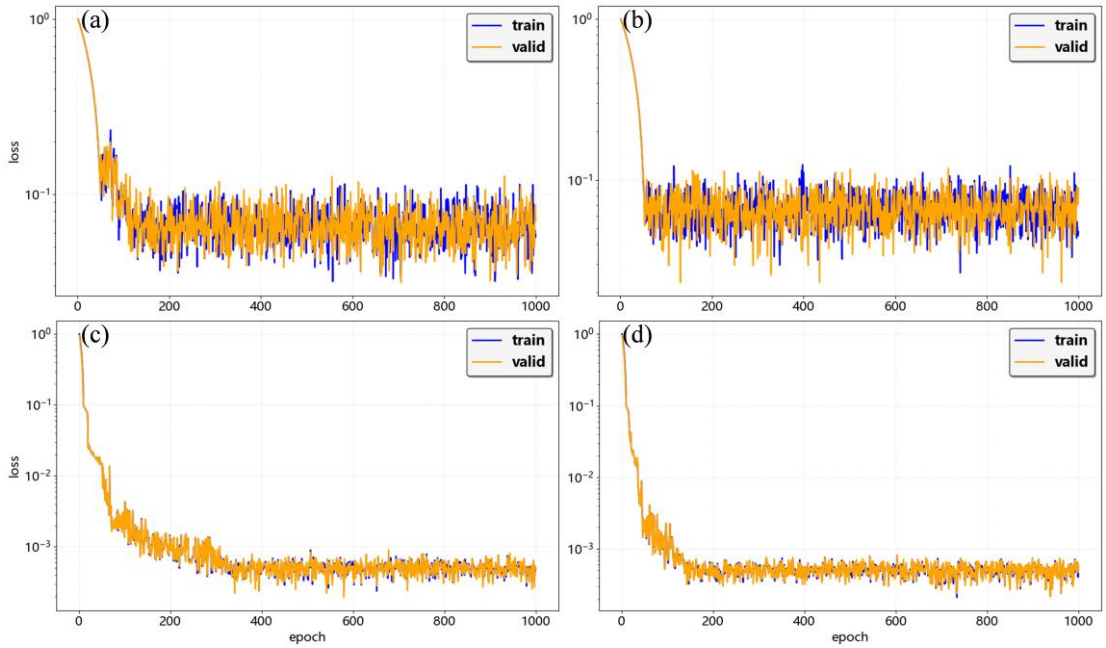

Figure 3. Loss function curves with and without transfer in training and validation sets (a) fault-free model without transfer learning; (b) fault-free model without transfer learning; (c) fault-free model with transfer learning; (d) fault-free model with transfer learning.

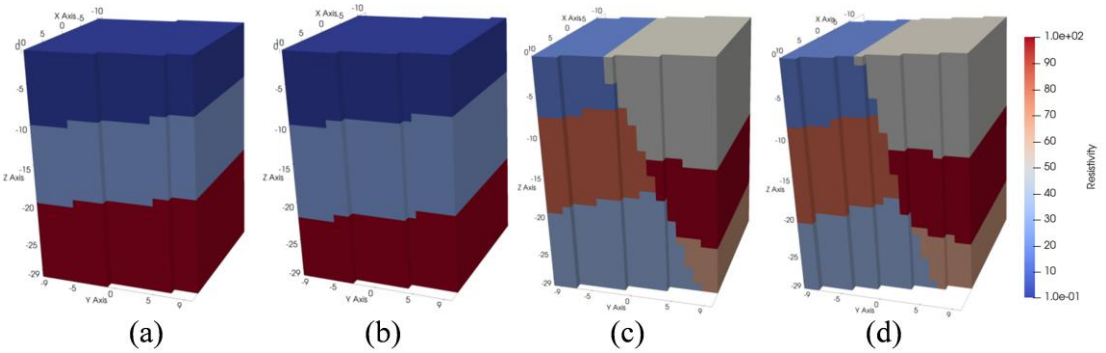

Figure 4. Fault-free and fault-free true and predictive models (a) fault-free true model; (b) fault-free predictive model; (c) fault-free true model; (d) fault-predictive model.

In this study, we construct two kinds of independent data sets: fault-free data set and fault-free data set, and analyze the effect of prior information completeness on cognitive uncertainty. Specifically, 3000 samples were taken as the baseline training set with 30% data volume, and the influence of data coverage improvement on the cognitive uncertainty trend was systematically investigated by gradually expanding the sample size to 6000(60%) and 10000(100%). In addition, in order to enhance the robustness of the deep learning inversion method to the actual measurement noise and study the relationship between different noise levels and arbitrary uncertainties, a noise enhancement strategy is adopted in this study. Weak noise (0.1 dB, 0.4 °), general noise (0.3 dB,1°) and strong noise (0.5 dB,2°) are superimposed on the amplitude ratio and phase difference signals respectively to evaluate

the response law of arbitrary uncertainties with noise intensity. The network model parameter settings are shown in Table 4.

Table 4. Network parameter settings for different data sets and noise levels

network name	the number of data sets	noise level	[Amplitude ratio, phase difference]
network A	3000	weak noise	$[0.1\text{dB}, 0.4^{\circ}]$
network B	6000	weak noise	$[0.1\text{dB}, 0.4^{\circ}]$
network C	10000	weak noise	$[0.1\text{dB}, 0.4^{\circ}]$
network D	10000	general noise	$[0.3\text{dB}, 1^{\circ}]$
network E	10000	strong noise	$[0.5\text{dB}, 2^{\circ}]$

Firstly, the noise in the training set is controlled to be weak noise (0.1 dB, 0.4 °), and then the network is trained with 3000, 6000 and 10000 data sets respectively. The trained networks are named network A, network B and network C respectively. The loss function curve is shown in Figure 5.

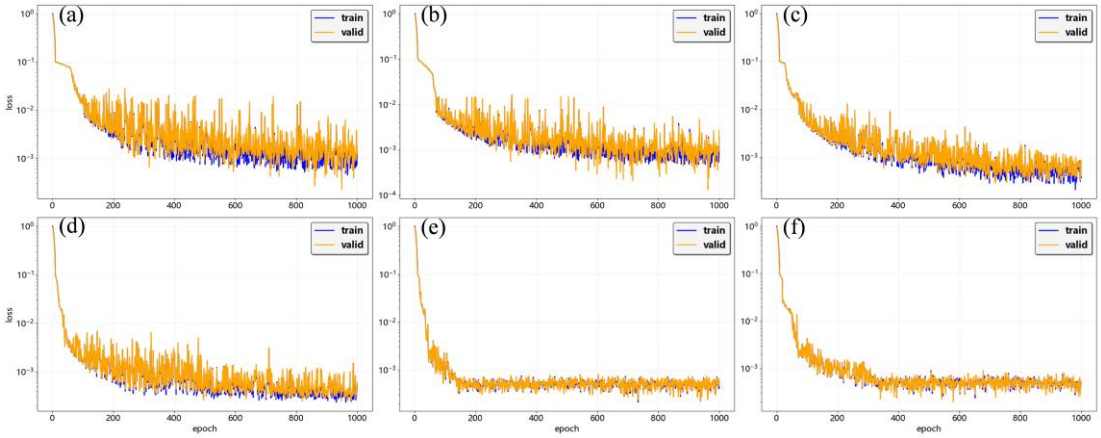

Figure 5. Graph of network training loss function for different datasets (a) Network A faultless dataset; (b) Network A fault dataset; (c) Network B faultless dataset; (d) Network B fault dataset; (e) Network C faultless dataset; (f) Network C fault dataset.

As can be seen from the graph of loss function in Figure 5, with the increase of data set size, the fitting effect of training set and validation set gradually improves, and finally tends to be unchanged. Based on networks A, B, C, the inversion results are evaluated using coefficients of determination. During validation, true parameter values are taken as abscissa coordinates, prediction parameter values as ordinate coordinates, and y = x function as reference. 20 models are randomly selected from the newly generated fault-free model and fault model for validation, so as to evaluate the performance of neural network after training. The validation results are shown in Figure 6.

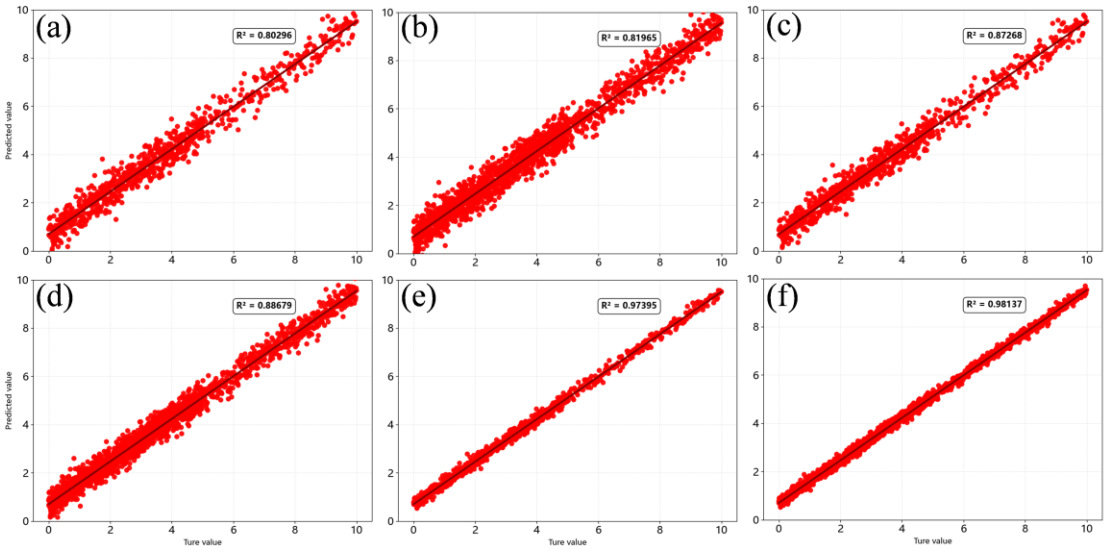

Figure 6. Validation set error analysis for networks with different datasets (a) Network A faultless dataset; (b) Network A fault dataset; (c) Network B faultless dataset; (d) Network B fault dataset; (e) Network C faultless dataset; (f) Network C fault dataset.

Then, 10000 training data sets are used to introduce complex noise disturbances of different intensities into the training set: weak noise (0.1 dB, 0.4 °), general noise (0.3 dB,1°) and strong noise (0.5 dB,2°). Based on the noisy training set, neural networks are trained respectively, and network C, network D and network E are obtained correspondingly. The evolution curve of the loss function during training is shown in Figure 7.

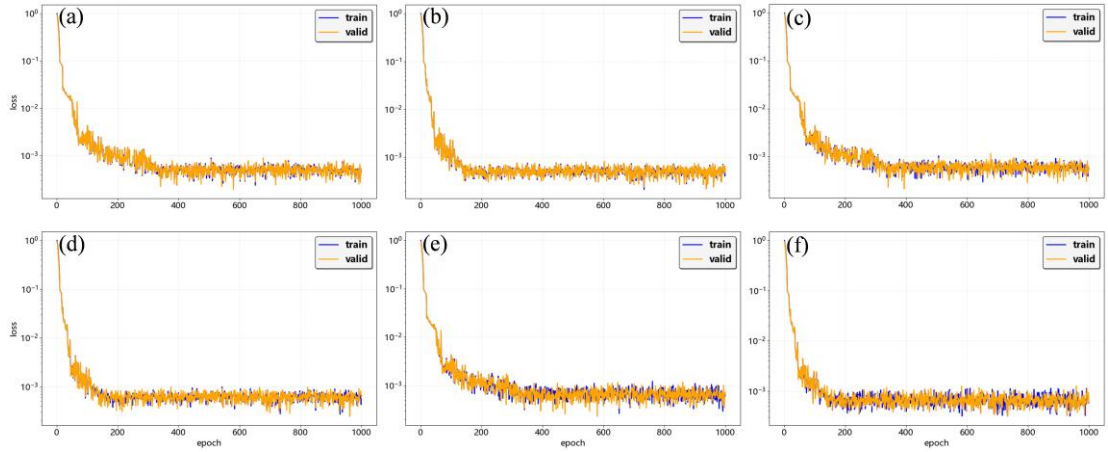

Figure 7. Training loss curves of networks at different noise levels (a) Network C faultless dataset; (b) Network C fault dataset; (c) Network D faultless dataset; (d) Network D fault dataset; (e) Network E faultless dataset; (f) Network E fault dataset.

In order to evaluate the generalization performance and anti-noise ability of the trained model, 100 models are randomly selected from the continuous and fault model sample library regenerated by networks C, D and E to form a validation set, and validation experiments are carried out. The validation results are shown in Figure 8. Even under strong noise training condition, the coefficient of determination of parameter error of validation set inversion is still above 0.9, which indicates that the 3D BNN model after transfer learning has excellent anti-noise robustness and can still maintain stable parameter inversion accuracy under complex noise interference scenes.

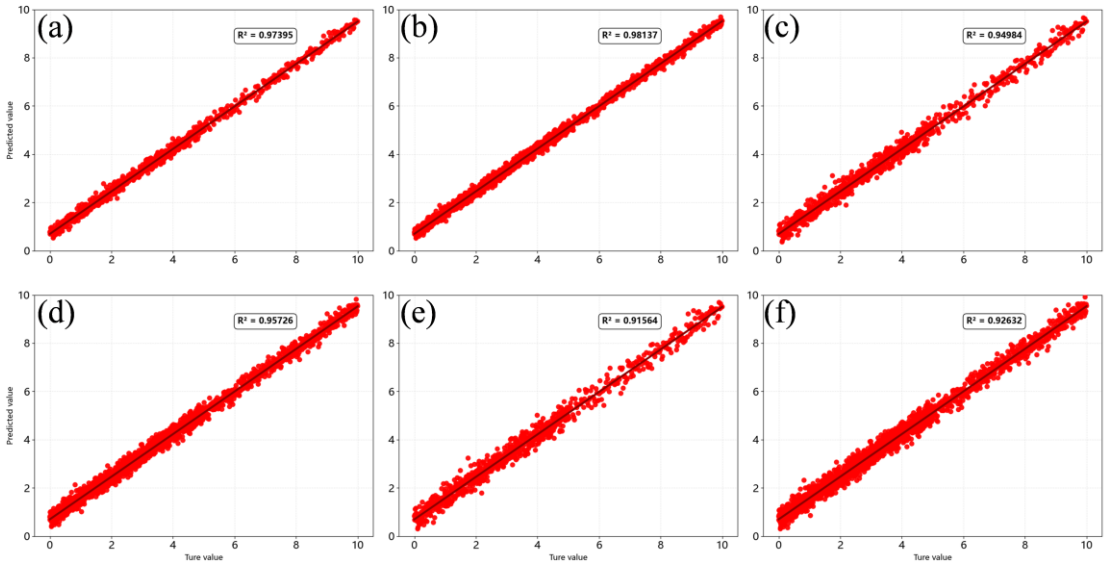

Figure 8. Error analysis of validation sets based on networks at different noise levels (a) Network C faultless dataset; (b) Network C fault dataset; (c) Network D faultless dataset; (d) Network D fault dataset; (e) Network E faultless dataset; (f) Network E fault dataset.

4. ANALYSIS OF INVERSION ALGORITHM

4.1. Numerical Examples

In order to simulate more complex geological scenes and verify the applicability of the method under complex structures, this study selects a 3D complex geological model with two inward dipping faults to carry out verification experiments. In order to achieve high-precision inversion of the whole model region, we divide the model into 20 independent partitions at equal intervals of 20m, and perform targeted inversion operations on each partition separately (as shown in Figure 9). Finally, through fusion and splicing of the independent inversion results of each subarea, the complete inversion results of the whole model are obtained to ensure the inversion accuracy and overall coherence of the complex structural area.

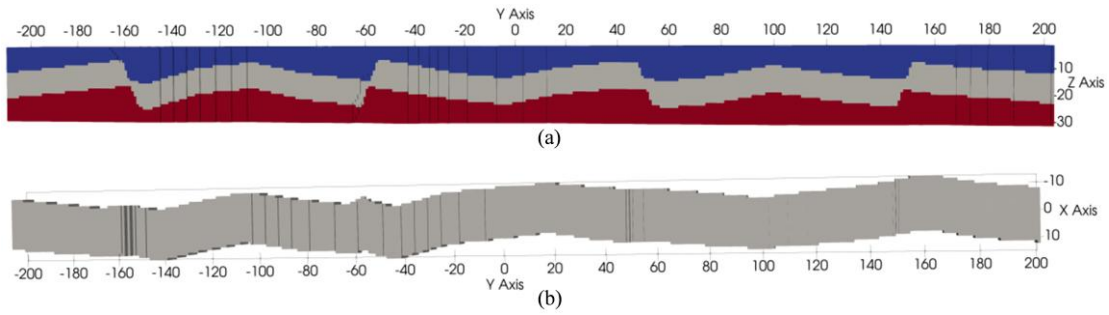

Figure 9. Three-dimensional graben fracture model diagram (a) YZ plane; (b)XY plane

4.2. Evaluation of Inversion Results

Firstly, the influence of the number of data sets on prediction accuracy is analyzed, and the forward responses of the two models are input into the networks A, B and C trained under the corresponding categories respectively to obtain the prediction parameters of each partition model. The predicted parameters of each subarea are integrated and filled into the three-dimensional grid to obtain a complete resistivity model, and then the inversion results of the whole test model are finally obtained by splicing in the order of models 1 to 20. The inversion results are shown in Figure 10.

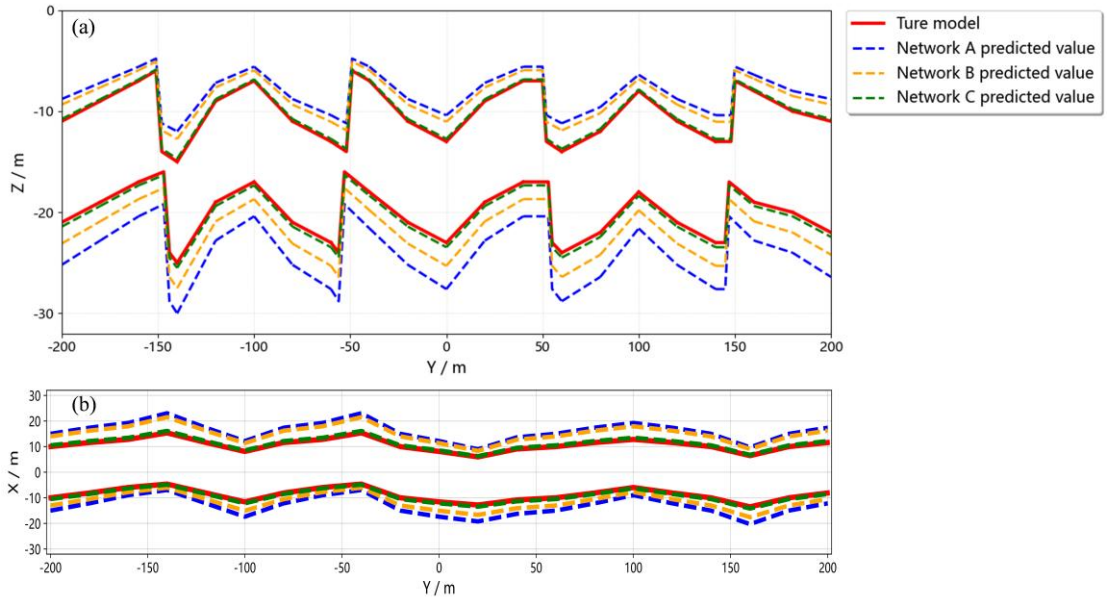

Figure 10. Model boundary prediction distributions based on networks of different data sets (a)YZ plane; (b)XY plane.

As can be seen from Figure 10, comparing the inversion effects of the three Bayesian neural networks, it is found that the fitting accuracy of network C is the best, indicating that when the data set is sufficient, the model can learn the formation electromagnetic response characteristics more fully, and the parameter prediction confidence is the highest. The fitting effects of networks A and B are relatively weak, and the dispersion degree is significantly increased. This result shows that when the number of data sets is small, the true electromagnetic response of the formation will be concealed, which will make it difficult for the model to accurately capture the response characteristics, and then cause poor inversion effect.

In order to analyze the relative error between the values of the parameters and the true values, the inversion results are further evaluated using the coefficient of determination and RMS error. As shown in Figure 11, the prediction accuracy of network C is the best, all greater than 0.96, indicating that the error between the predicted value and the true value is small.

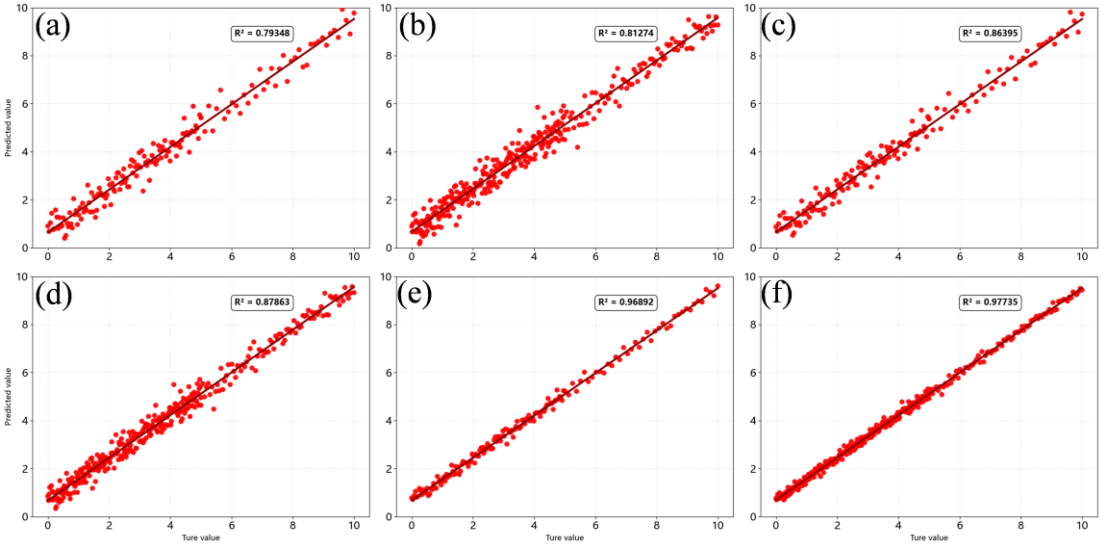

Figure 11. Parameter evaluation of test sample models based on networks A, B, and C (a) network A faultless dataset; (b) network A faultless dataset; (c) network B faultless dataset; (d) network B faultless dataset; (e) network C faultless dataset; and (f) network C faultless dataset.

The RMS values were used to quantify the errors between the predicted and true values for each parameter in the test case. The distribution is shown in Figure 12. It can be seen that Network C has the smallest RMS value and the RMS value is significantly lower than Network A and Network B. It shows that the inversion effect of network C is obviously better than the other two networks, and the number of training data sets has a great influence on the inversion result of network training.

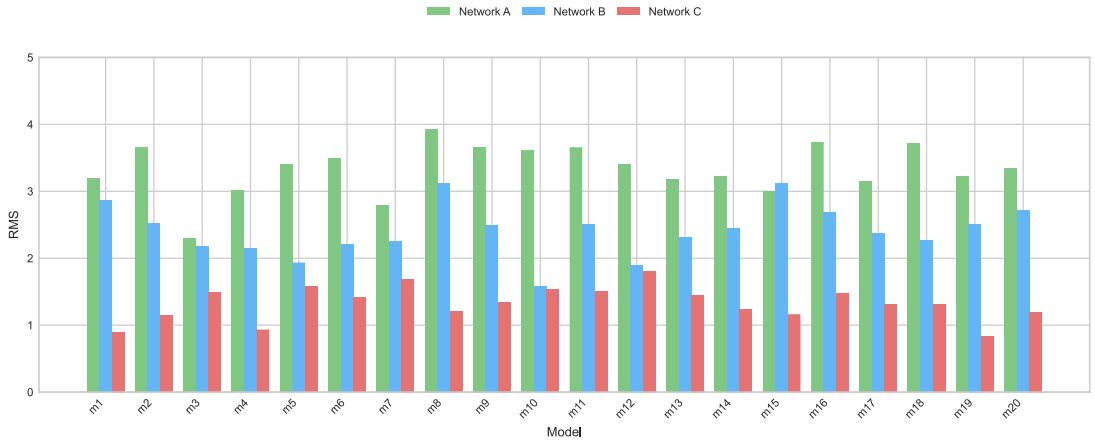

Figure 12. RMS values for test samples based on networks A, B, and C

Networks C, D and E are tested by adding different levels of noise to analyze the robustness of different noise to deep learning inversion networks. The forward responses of the two classes of models are input into the networks C, D and E trained under the corresponding classes respectively, and the prediction parameters of each partition model are obtained. The single resistivity model is obtained by integrating the filling prediction parameters, and then the inversion results of the whole test model are obtained by splicing the models 1 to 20 in the order, and the inversion results are shown in Figure 13.

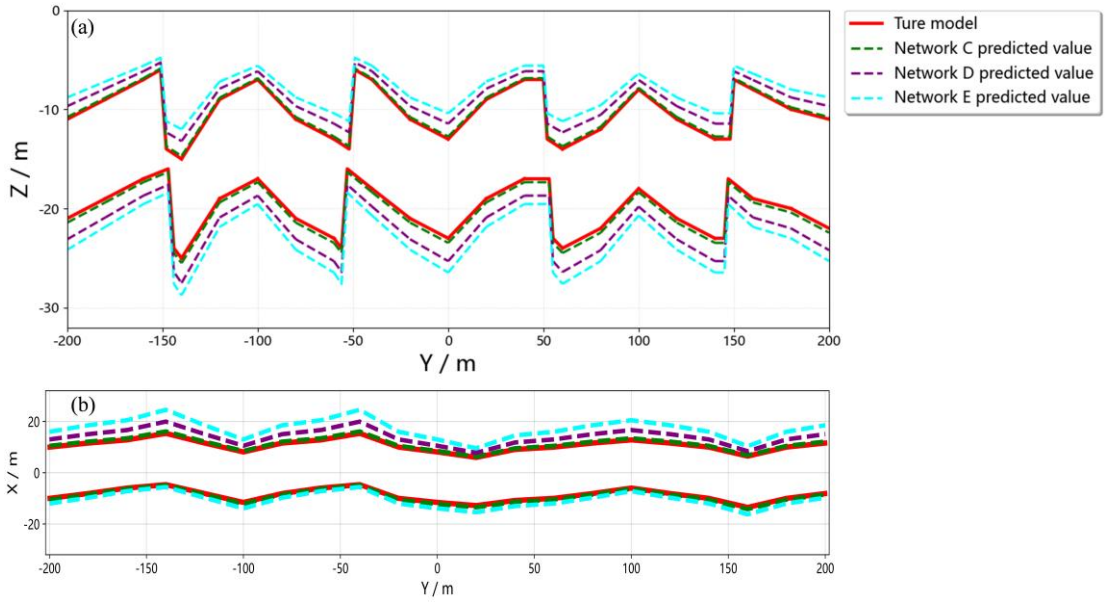

Figure 13. Model boundary prediction distributions based on different noise networks (a)YZ plane; (b) XY plane.

As shown in Figure 13, for the same number of data sets, network C has the best boundary fitting accuracy, network D is second, and network E has the weakest fitting degree. This phenomenon indicates that the increase of noise intensity will amplify the random error of prediction, resulting in poor inversion effect. The coefficient of determination is used R^2 to further verify that, as shown in Figure 14, the coefficients of the three networks R^2 remain above 0.9, which proves that the

robustness and generalization ability of the deep learning inversion network after transfer learning are strong.

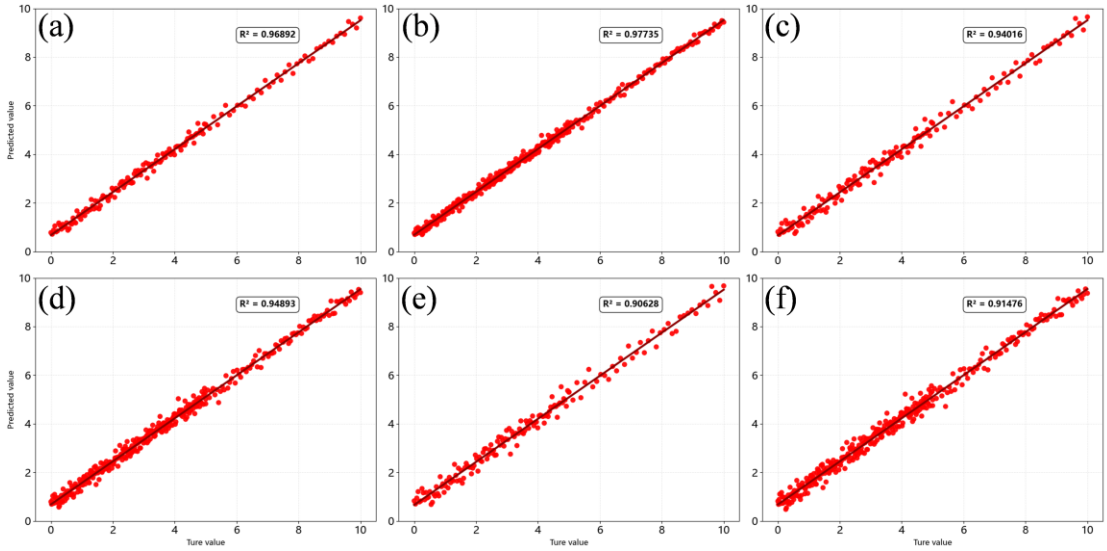

Figure 14. Test sample model parameter evaluation based on Network C, Network D, and Network E (a) Network C fault-free dataset; (b) Network C fault dataset; (c) Network D fault-free dataset; (d) Network D fault dataset; (e) Network E fault-free dataset; (f) Network E fault dataset.

4.3. Two Uncertainty Assessments

Cognitive uncertainty and arbitrary uncertainty are the core indexes of Bayesian neural network for predicting randomness quantitatively. Cognitive uncertainty arises from insufficient prior information, incomplete data coverage, or incomplete learning of complete features by the model. Arbitrary uncertainty is caused by measurement noise, instrument interference and randomness of the formation itself, independent of the amount of training data.

First, the relationship between the number of data sets and cognitive uncertainty is analyzed, and the cognitive uncertainty distribution results based on networks A, B, and C are shown in FIG. 15A. It can be seen that network A has the highest cognitive uncertainty: due to insufficient training data coverage, the network is difficult to fully learn complex three-dimensional features, resulting in posterior distribution divergence. The uncertainty of network B decreases obviously: the increase of data makes the model better capture spatial structure features, and the cognitive ambiguity decreases. Network C has the least cognitive uncertainty and the most centralized distribution: it shows that BNN can effectively learn the mapping relationship between underground electromagnetic response and formation structure from data when the training set covers enough, and the prior uncertainty is significantly reduced. The smaller the cognitive uncertainty, the better the inversion effect of the network.

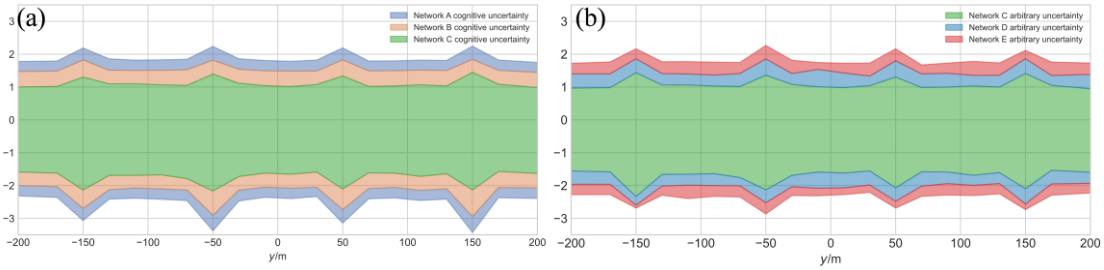

Figure 15. Two uncertainty distributions: (a) cognitive uncertainty distributions for networks A, B, and C; (b) arbitrary uncertainty distributions for networks C, D, and E.

Finally, the relationship between noise intensity and arbitrary uncertainty in the data set is analyzed, and the distribution diagram of arbitrary uncertainty estimation based on networks C, D and E is shown in FIG. 15(b). Network C has minimum arbitrary uncertainty: input signal interference is weak, prediction distribution is concentrated. The arbitrary uncertainty of network D is obviously increased: noise interference is enhanced, and the posterior distribution of inversion parameters is widened. Network E has the highest arbitrary uncertainty and the widest distribution: strong noise severely corrupts the input signal, causing significant amplification of prediction uncertainty. This law shows that the noise intensity is positively correlated with arbitrary uncertainty, and the inversion parameter accuracy decreases gradually with the increasing noise, while the arbitrary uncertainty increases continuously, which directly reflects the influence of the measured signal quality on the inversion reliability.

The results of this section show that Bayesian neural network can be used to evaluate uncertainty in deep learning inversion. Cognitive uncertainty and arbitrary uncertainty estimation methods can be used to measure non-uniqueness problems caused by insufficient prior information of the model and inherent noise of the data while reconstructing the subsurface resistivity model. By example analysis, the model with fault and model without fault can be distinguished by using cognitive uncertainty estimation, and it is proved that other data besides the distribution of training set can be distinguished by using cognitive uncertainty estimation.

5. CONCLUSIONS

Aiming at the key problems of large computation amount, scarce data and obvious noise interference in 3D electromagnetic inversion while drilling, a migration learning inversion method is proposed and a 3D resistivity inversion framework integrated with Bayesian neural network is constructed. Through 2D pretraining-3D fine tuning strategy, the electromagnetic bottom layer characteristics are migrated. Under the same 3D sample size, the strategy can make the loss value converge from 0.1 without migration to 0.001 with migration, and the iteration times are reduced by 80%. significantly reduce that training cost and improve the stability of the model; meanwhile, the parameter prediction determination coefficient of the three-dimensional BNN model are all greater than 0.9 under weak, general and strong noise conditions, and the three-dimensional BNN model has excellent anti-noise ability; moreover, the fault position and the stratum boundary of the inclined fault graben model can be accurately restored by adopting the strategy of subarea inversion and result splicing; combined with uncertainty analysis, the core mechanism that the cognitive uncertainty decreases with the increase of data amount and the arbitrary uncertainty increases with the increase of noise intensity is revealed; It provides quantitative basis for model credibility evaluation and risk control. This method has obvious advantages in reducing data demand,improving inversion efficiency, enhancing anti-noise robustness and quantifying uncertainty,etc. It can provide high-precision, interpretable and engineerable inversion scheme for real-time geological exploration under complex geological conditions.

REFERENCES

[1] Kang Z, Zhang Y, Qin H, et al. An intelligent inversion method for azimuth electromagnetic logging while drilling measurements [J]. IEEE Access, 2023, 11: 79285-79294.

[2] Wang Nanzhe, Chang Haibin, Zhang Dongxiao. Deep-Learning-Based Inverse Modeling Approaches: A Subsurface Flow Example [J]. Journal of Geophysical Research: Solid Earth, 2021, 126(2): e2020JB020549.

[3] Jin Y, Wu X, Chen J, et al. A physics-driven deep learning network for subsurface inversion [C]//2019 United States National Committee of URSI National Radio Science Meeting (USNC-URSI NRSM). IEEE, 2019: 1-2.

[4] LIU B, GUO Q, LI S, et al. Deep Learning Inversion of Electrical Resistivity Data [J]. IEEE Transactions on Geoscience and Remote Sensing, 2020, 58(8): 5715-5728.

[5] Wu X, Shi Y, Fomel S, et al. 2019b. FaultNet3D: Predicting fault probabilities, strikes, and dips with a single convolutional neural network [J]. IEEE Transactions on Geoscience and Remote Sensing, 57(11): 9138–9155.

[6] Gao K, Huang L, Zheng Y. Fault detection on seismic structural images using a nested residual U-Net [J]. IEEE Transactions on Geoscience and Remote Sensing, 2021, 60: 1-15.

[7] Ma X, Yao G, Zhang F, et al. 3-D seismic fault detection using recurrent convolutional neural networks with compound loss [J]. IEEE Transactions on Geoscience and Remote Sensing, 2023, 61: 1-15.

[8] Shan Z, Ling D, Xie Z, et al. A semianalytical solution for one-dimensional transient wave propagation in a saturated single-layer porous medium with a fluid surface layer [J]. International Journal for Numerical and Analytical Methods in Geomechanics, 2019, 43(13): 2184-2199.

[9] Cui Z D, Zhang Z L, Yuan L, et al. Design of underground structures [M]. Springer Singapore, 2020.

[10] PUZYREV V. Deep learning electromagnetic inversion with convolutional neural networks [J]. Geophysical Journal International, 2019, 218(2): 817-832.

[11] Hu Y, Guo R, Jin Y, et al. A supervised descent learning technique for solving directional electromagnetic logging-while-drilling inverse problems [J]. IEEE Transactions on Geoscience and Remote Sensing, 2020, 58(11): 8013-8025.

[12] Noh K, Pardo D, Torres-Verdín C. Physics-guided deep-learning inversion method for the interpretation of noisy logging-while-drilling resistivity measurements [J]. Geophysical Journal International, 2023, 235(1): 150-165.

[13] Zhao Ning, Shen Songning, Li Ning, et al. Deep learning inversion of ultra-deep azimuthal electromagnetic logging while drilling based on physical driving [J]. Petroleum Geophysical Exploration, 2024, 59(5): 1069-1079.

[14] Dominguez-Cruz M A, España-Pinto J A, Valdiviezo-Mijangos O C, et al. Petroelastic modeling of well logging and seismic inversion data combining rock physics templates and conventional petrophysical analysis for 1D, 2D, and 3D supervised reservoir characterization of the Stybarrow Field in Exmouth sub-basin inner Carnarvon Basin, Australia [J]. Modeling Earth Systems and Environment, 2025, 11(2): 97.

[15] Noh K, Pardo D, Torres-Verdín C. 2.5-D deep learning inversion of LWD and deep-sensing EM measurements across formations with dip faults [J]. IEEE Geoscience and Remote Sensing Letters, 2021, 19: 1-5.

[16] Zhao N, Li N, Xiao Z, et al. Physics-driven deep learning pixel-based inversion of logging while drilling in anisotropic formation [J]. IEEE Transactions on Geoscience and Remote Sensing, 2024, 62: 1-12.

[17] Qin H, Kang Z, Chen R, et al. A novel inversion method of logging while drilling azimuthal electromagnetic data in anisotropic formations based on BiLSTM [J]. Journal of Geophysics and Engineering, 2025: gxaf063.

[18] Jamil A. Machine Learning Methods for 2D Electrical Resistivity Inversion Applied to Hydrogeological Subsurface Characterization[D]. New Mexico State University, 2025.

[19] Singh S K. Optimising mobile laser scanning for underground mines [D]. University of New South Wales (Australia), 2022.

[20] Liu Y, Yin C, Qiu C, et al. 3-D inversion of transient EM data with topography using unstructured tetrahedral grids [J]. Geophysical Journal International, 2019, 217(1): 301-318.

[21] Maleki F, Ovens K, Gupta R, et al. Generalizability of machine learning models: quantitative evaluation of three methodological pitfalls [J]. Radiology: Artificial Intelligence, 2022, 5(1): e220028.

[22] Puzyrev V, Swidinsky A. Inversion of marine electromagnetic data using a deep learning-based approach with transfer learning [J]. Geophysical Journal International, 2022, 231(1): 214-229.

[23] Yosinski J, Clune J, Bengio Y, et al. How transferable are features in deep neural networks? [J]. Advances in neural information processing systems, 2014, 27.

[24] Zhang Z, Alkhalifah T. High-resolution reservoir characterization using deep learning-aided elastic full-waveform inversion: The North Sea field data example [J]. Geophysics, 2020, 85(4): WA137-WA146.

[25] Gooneratne C P, Li B, Deffenbaugh M, et al. Instruments, measurement principles and communication technologies for downhole drilling environments [M]. Cham, Switzerland: Springer International Publishing, 2019.

[26] Kaura A M, Andrawus Y, Ibrahim A Y. Geophysics, Geology, Formation Evaluation, and Reservoir Characterization in Unconventional Resources [M]//Unconventional Resources. CRC Press, 2025: 40-122.

[27] Yang Xuemin, Peng Chengbin. A new seismic steering drilling technology for reducing drilling risk and increasing reservoir penetration rate [J]. Petroleum Exploration, 2018, 57 (04):627-636.

[28] Liu Cheng. Challenges and countermeasures of wellbore stability control by drilling fluid in extended reach wells [J]. Petrochemical Technology, 2024, 31 (11):256-258+275.

[29] Gal Y, Ghahramani Z. Dropout as a bayesian approximation: Representing model uncertainty in deep learning [C]//international conference on machine learning. PMLR, 2016: 1050-1059.

[30] Kendall A, Gal Y. What uncertainties do we need in bayesian deep learning for computer vision? [J]. Advances in neural information processing systems, 2017, 30.

[31] Oh S, Byun J. Bayesian uncertainty estimation for deep learning inversion of electromagnetic data [J]. IEEE Geoscience and Remote Sensing Letters, 2021, 19: 1-5.